ACS NANO

www.acsnano.org

ARTICLE

Reducing Nonradiative Losses in Perovskite LEDs through Atomic Layer Deposition of Al_2O_3 on the Hole-Injection Contact

Emil G. Dyrvik, Jonathan H. Warby, Melissa M. McCarthy, Alexandra J. Ramadan, Karl-Augustin Zaininger, Andreas E. Lauritzen, Suhas Mahesh, Robert A. Taylor, and Henry J. Snaith*

Cite This: *ACS Nano* 2023, 17, 3289−3300

Read Online

ACCESS | Metrics & More | Article Recommendations | Supporting Information

ABSTRACT: **Halide perovskite light-emitting diodes (PeLEDs) exhibit great potential for use in next-generation display technologies. However, scale-up will be challenging due to the requirement of very thin transport layers for high efficiencies, which often present spatial inhomogeneities from improper wetting and drying during solution processing. Here, we show how a thin Al_2O_3 layer grown by atomic layer deposition can be used to preferentially cover regions of imperfect hole transport layer deposition and form an intermixed composite with the organic transport layer, allowing hole conduction and injection to persist through the organic hole transporter. This has the dual effect of reducing nonradiative recombination at the heterojunction and improving carrier selectivity, which we infer to be due to the inhibition of direct contact between the indium tin oxide and perovskite layers. We observe an immediate improvement in electroluminescent external quantum efficiency in our p-i-n LEDs from an average of 9.8% to 13.5%, with a champion efficiency of 15.0%. The technique uses industrially available equipment and can readily be scaled up to larger areas and incorporated in other applications such as thin-film photovoltaic cells.**

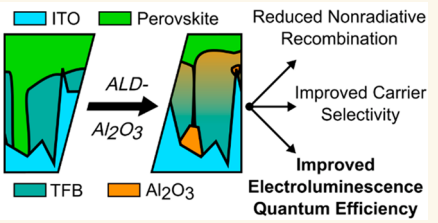

KEYWORDS: *perovskite, light-emitting diode, atomic layer deposition, area selective, efficiency*

INTRODUCTION

Halide perovskite semiconductors have attracted enormous interest from the scientific community and industry over the past decade. A large variety of applications for this group of materials are being explored, including photovoltaic cells,[1] radiation detectors,[2] light-emitting diodes (LEDs),[3] lasers,[4] and photodetectors.[5] Halide perovskites are interesting for LED applications, since they have highly efficient, tunable emission, with a narrow emission spectrum, and could feasibly outperform organic LEDs (OLEDs) in terms of absolute efficiency, due to the process of photon recycling.[6−9] Since the report of the first room-temperature halide perovskite light-emitting diode (PeLED) in 2014,[3] both publication numbers and efficiencies have soared. External quantum efficiencies of electroluminescence (EQE_{EL}) above 20% have been reported by multiple groups since 2018.[10−13] The rapid rise in efficiencies has been achieved through numerous improvements in design and fabrication, such as carrier confinement in the emitter,[14−16] defect passivation strategies,[17−19] improved carrier injection and transport,[20−22] and thermal management strategies.[20,23]

PeLED devices are typically designed in both positive−intrinsic−negative (p-i-n) or negative−intrinsic−positive (n-i-p) heterostructure architectures with the emissive perovskite layer sandwiched between a hole transport layer (HTL) and an electron transport layer (ETL). An important property of the charge transport layer (CTL), and the contact that it forms in the device, is its "selectivity" for one carrier type, which can be defined as $S_e = \rho_{c,h}/(\rho_{c,h} + \rho_{c,e}) = 1 - S_h$, where S_e is the electron selectivity of the contact, S_h is the hole selectivity, and $\rho_{c,h}$ and $\rho_{c,e}$ are the resistivities to hole and electron conduction through the contacts, respectively.[24] It follows that a good CTL should be highly conductive for the majority carrier while being highly resistive for the minority carrier.

Organic HTLs in p-i-n device structures are typically deposited on transparent conducting oxides (TCOs) by spin-coating. Ideally, the CTL should provide full coverage of the TCO surface to reduce nonradiative recombination at the TCO−perovskite interface that would also cause a lack of

Received: May 16, 2022
Accepted: February 10, 2023
Published: February 15, 2023

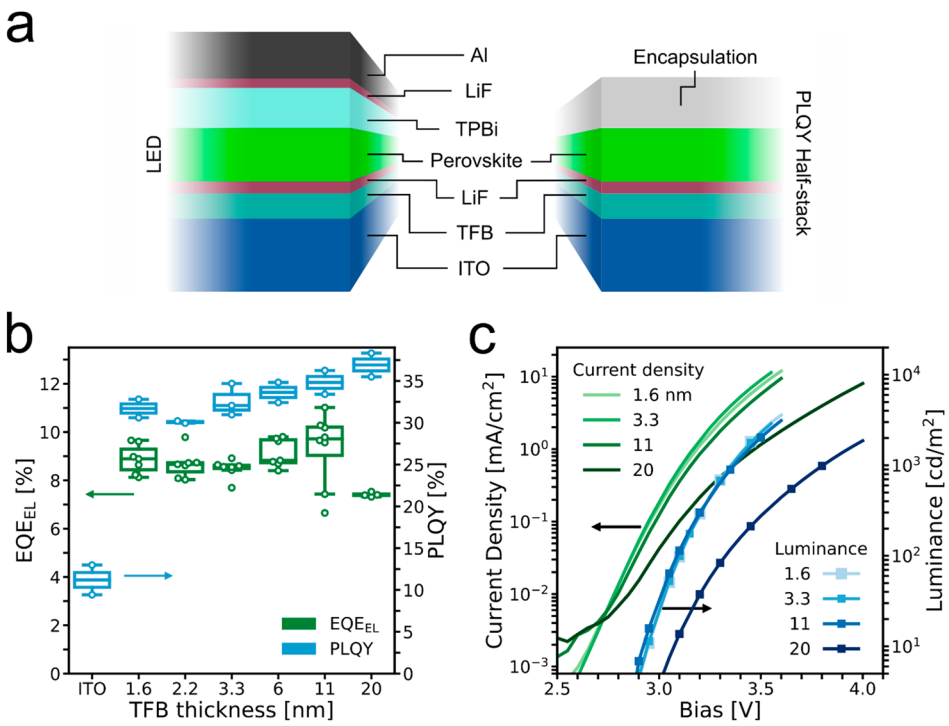

Figure 1. (a) Architecture of LED devices and half-stack samples for PLQY measurements. Thicknesses are not to scale. (b) Devices with varying TFB layer thicknesses and no Al_2O_3 interlayer. EQE_{EL} values are the highest recorded EQE_{EL} for each device, and PLQY values are the average value per sample. (c) J–V–L characteristics of representative devices with varying TFB layer thicknesses.

selectivity of the contact due to a leakage of oppositely charged carriers from the emissive layer. Furthermore, the CTLs should be as thin as possible to reduce series resistance, which can cause loss due to Joule heating. In addition, the thicknesses of the HTL and ETL require optimization such that the hole and electron currents to the perovskite emitter match each other, facilitating efficient bimolecular recombination.[9] The optical outcoupling efficiency (OOE) of the emitted light also depends on the refractive indices (n), extinction coefficients (k), and thicknesses of the constituent layers of the device. A device with a high internal electroluminescent quantum efficiency can have a relatively poor EQE_{EL} if the device stack (i.e., the perovskite and CTL thicknesses) is not optimized for a high outcoupling efficiency. It is clear to see that it is a significant challenge to balance all of these considerations to make high-efficiency devices.

Atomic layer deposition (ALD) is a layer-by-layer deposition technique which is surface controlled, allowing monolayer control of film growth.[25−27] The ALD process consists of sequential, self-limiting surface reactions as alternating precursors and coreactants are introduced, separated by a purge of an inert gas. An ALD cycle may then be repeated to increase the number of layers and thus the thickness of the thin film deposited. Adequate reactive sites are required on the substrate surface for the precursor to react with, ensuring the self-limiting nature. If no reactive sites are available, no further deposition can take place. The uniformity and unparalleled conformality provided by this technique have led to its favored use in the scaling down of microelectronics.[25,28−30] The low-temperature deposition and mild technique has also led to its application in perovskite solar cells[31−36] as well as deposition on temperature-sensitive polymers.[37−42]

Area-selective ALD (AS-ALD) takes advantage of the strong dependence of ALD on surface chemistry, where the commencement of growth is conditional to the substrate surface.[43,44] Here, deposition is limited to specific substrate areas, enabling predefined patterns to be established for bottom-up processing.[45−52] Unreactive polymers[53−57] as well as self-assembled monolayers (SAMs)[58−60] have been used to allow surface modification and to mask selective reactive areas to prevent ALD growth. These materials act as a physical barrier, preventing the ALD precursor from reacting with substrate surface reactive groups. For unreactive polymers in this system, adequate ALD purges are required to inhibit the gaseous precursor from diffusing into the porous material and reaching the underlying substrate. If a sufficient purge is not applied, or if molecules become trapped in the porous polymer, these precursor molecules may then react with subsequent ALD precursors, leading to a delayed nucleation and eventual growth.[39,61]

In this work we develop a composite hole-injection layer composed of poly(9,9-dioctylfluorene-*alt*-*N*-(4-*sec*-butylphenyl)diphenylamine) (TFB) and Al_2O_3. We employ principles from AS-ALD to form an intermixed TFB–Al_2O_3 layer that blocks pinholes and thus inhibits nonradiative recombination sites in the interface between the perovskite and the hole-injection/electron-blocking layer. The result is an ultrathin transport layer with a very high resistivity to electrons, while efficiently injecting holes. Our champion LED efficiency improves from 12 to 15% EQE_{EL}, confirming the improved properties of the composite hole-injection layer.

RESULTS AND DISCUSSION

For the green perovskite emitter, we employ the commonly used[15,16,20,62−65] material $CsPbBr_3$ within a phenylethylammonium bromide rich (PEABr) matrix, processed as we have previously reported.[64] The emission wavelength varies depend-

https://doi.org/10.1021/acsnano.2c04786
ACS Nano 2023, 17, 3289−3300

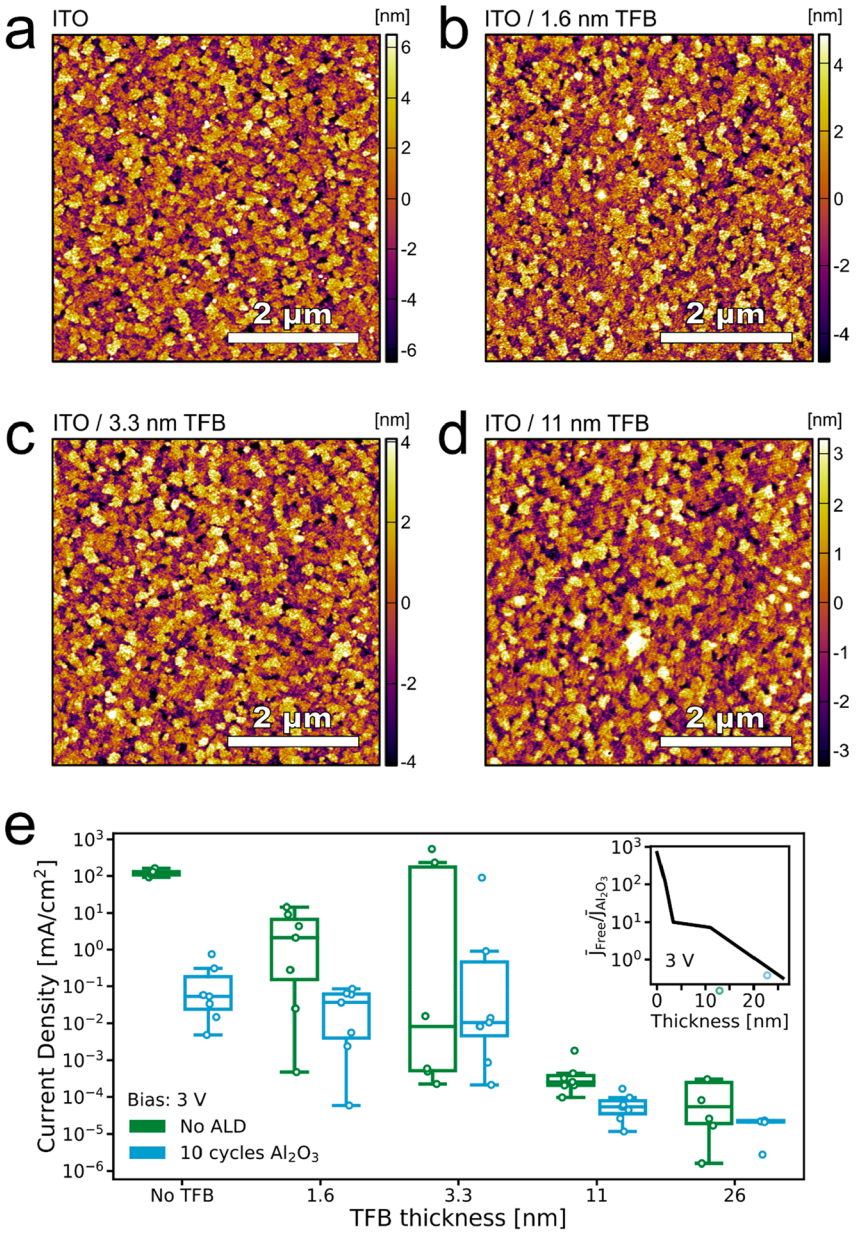

Figure 2. AFM micrographs of the topography of (a) the ITO surface, (b) ITO with 1.6 nm (0.5 mg/mL) TFB layer, (c) ITO with 3.3 nm (2 mg/mL) TFB layer, and (d) ITO with 11 nm (5 mg/mL) TFB layer. (e) Current density snapshot at 3 V bias for "electron-only" unipolar devices with varying TFB thicknesses and with or without the Al_2O_3 interlayer. In the inset in (e), the ratio of the mean of the current densities at 3 V for the Al_2O_3-free and Al_2O_3-covered samples is plotted as a function of TFB thickness.

ing upon the PEABr content. With 40 mol % excess PEABr in comparison to the CsBr, the wavelength sits within the green emission channel, with a PL peak position of 518 nm (Figure S1 in the Supporting Information).

We integrate the emission layer in LEDs with a p-i-n architecture of ITO/poly(9,9-dioctylfluorene-*alt*-*N*-(4-*sec*-butylphenyl)diphenylamine) (TFB)/LiF/perovskite/2,2′,2″-(1,3,5-benzinetriyl)-tris(1-phenyl-1*H*-benzimidazole) (TPBi)/LiF/Al (Figure 1a). Using a similar structure, we have previously achieved an EQE_{EL} of up to 12% but observed a photoluminescence quantum yield (PLQY) of up to 28% from the same complete device stack.[64] The discrepancy between EQE_{EL} and PLQY suggests there is an unrealized potential for higher efficiency in our devices. To improve the operating efficiency of the LEDs in this work, we adapt the HTL to optimize the hole-injection and electron-blocking nature of the p-side of the device.

To investigate how sensitive the LED performance is to the thickness of the hole-transport layer, we start by varying the thickness of the TFB layer by changing the concentration of TFB in the spin-coated solution and measure the PLQY on encapsulated "half-stacks" (ITO/HTL/LiF/perovskite) and EQE_{EL} of devices (Figure 1b). When the thickness of the TFB film is increased, the PLQY continues to increase, from an average of 32% for 1.6 nm TFB thickness to 37% at 20 nm thickness, whereas the EQE_{EL} drops off when the TFB thickness exceeds 11 nm. Samples with TFB films thinner than 11 nm all yield progressively lower PLQY and EQE_{EL}, but even

https://doi.org/10.1021/acsnano.2c04786
ACS Nano 2023, 17, 3289−3300

the thinnest TFB layer in conjunction with the LiF layer enables significantly higher PLQY than the perovskite on the bare ITO surface, with 32% versus 11% PLQY. The procedure for determining the thickness of the films is outlined in Note 1 in the Supporting Information.

Figure 1c shows the voltage dependence of the current density and luminance (J–V–L) of representative devices for each thickness. The device with the thickest TFB shows a strong reduction in both current density and luminance compared with those of the thinner ones. Among the three other devices there is almost no difference in luminance, but the current densities in the devices with the thinnest TFB films are slightly higher than that for the more efficient device with 11 nm TFB. The EQE_{EL} as a function of current density is given in Figure S3 in the Supporting Information.

A comparison of PLQY and EQE_{EL} provides valuable insights into the causes for emission losses, because PLQY does not rely on carrier transport and injection to deliver carriers to the emitter; thus, current transport losses and recombination losses can be uncoupled. In Figure 1b, we observe a general trend of increasing PLQY with increasing TFB thickness. This is consistent with the possible formation of "pinholes" in thinner TFB films. Contact between the perovskite emission layer with degenerately doped ITO would increase nonradiative recombination at the interface, leading to a reduction in emission, and, under bias, cause reduced selectivity, since electrons would be able to freely flow from the perovskite layer into the ITO. When the TFB thickness is increased, we assume the coverage over the ITO improves and reduced nonradiative recombination at this interface would lead to improvements in PLQY. If this is the case, there is a potential to improve the EQE_{EL} of devices with thinner TFB films compared to what we have achieved so far, by enabling improved coverage of the ITO. Notably, when we increase the TFB thickness above 11 nm, we observe a significant reduction in the injection current density under forward bias and a drop in the EQE_{EL}. It is likely that this originates from either (a) an increased series resistance for hole injection, resulting in an imbalance of electrons and hole current flow through the device, or (b) a reduction in optical outcoupling, with thicker HTLs. An increase in series resistance for hole injection would only reduce EQE_{EL} and not PLQY, whereas a reduction in optical outcoupling should reduce both. We observe a monotonic increase in PLQY with increasing TFB layer thickness; however, we do acknowledge that our PLQY measurements are on half-stacks and could thus have a different outcoupling dependency on the thickness. Variations in thickness of this magnitude have been shown to result in changes in outcoupling efficiency.[66] The concurrent reduction in current density with increased TFB thickness implies increased hole-injection resistance to be the primary factor reducing the EQE_{EL} for devices incorporating the thickest TFB layers.

Identifying Nonradiative Recombination Pathways and Improving Carrier Selectivity. To improve our understanding of the device performance, we investigate the morphology of the relevant layers in the device. We inspected the ITO and TFB layers by scanning electron microscopy (SEM) but were not able to discern any notable difference, possibly due to the penetration depth of the electron beam (Figure S4 in the Supporting Information). We then measured the topography using atomic force microscopy (AFM). Comparing scans of the ITO surface (Figure 2a) with scans of TFB thin films on ITO (Figure 2b–d), no clear difference can be discerned. The TFB thin films all display a topography similar to that of the bare ITO, suggesting a conformal deposition of the polymer. There is, however, a decrease in the root-mean-square roughness (RMS) of the TFB thin films with increasing film thickness (Table 1). The RMS roughness of the underlying ITO surface, at 3.3 nm, is in the same range as the thickness we measured of the thinner TFB layers employed. The reduction in roughness suggests that the TFB is partially planarizing the ITO substrate. Since the TFB thickness, for the thinner layers, is in the same range or less than the substrate roughness, it is likely that there will be some uncovered regions of ITO. Such uncovered regions protruding the TFB layer could act as contact points with the subsequently deposited perovskite emission layer.

Table 1. Root-Mean-Square Roughness of Surfaces in Figure 2a–d Determined by AFM

stack	roughness (nm)
ITO	3.3
ITO/1.6 nm TFB	2.7
ITO/3.3 nm TFB	2.3
ITO/11 nm TFB	1.7

With this potential for the presence of pinholes in the TFB layer, we suspect that the resulting ITO–perovskite interface that can form is increasing nonradiative recombination losses and decreasing the hole selectivity of the positive contact in our devices. To increase our understanding of how the TFB thickness may affect the selectivity of the positive contact, we construct unipolar, "electron-only" devices with the TFB layer sandwiched between two electron-selective contacts (Figure S5 in the Supporting Information).

In this configuration, the ITO/SnO_2 contact should effectively block hole transport. This means the measured current flowing through the device should be due to electrons traveling through the entire device stack primarily, injected through the TPBi, passing through the SnO_2, and collected at the ITO electrode. When sandwiching a hole-selective material such as TFB between the SnO_2 and TPBi, we expect to see a reduction in measured current density due to the reduced electron transport through the thin-film stack. We do not expect to observe any hole injection from the ITO/SnO_2 contact and hence only consider the electron current. TFB layers with incomplete coverage should still allow a substantial electron current because of the bare SnO_2/TPBi interfaces. As such, this device configuration allows us to assess the completeness of the HTL layer coating in a more quantitative manner.

When we scan these unipolar devices (Figure S6 in the Supporting Information), we see a difference in current density of roughly 6 orders of magnitude between the thickest TFB layer and the devices without any TFB. Figure 2e shows the current densities of all devices at 3 V bias. The presence of 1.6 and 3.3 nm TFB layers decreases the current density by a few orders of magnitude but shows large variability between devices (green boxes in Figure 2e). For 11 nm and above the variability is smaller and the current density is significantly suppressed.

Having identified clear evidence for current leakage through the thinner TFB layers, we hypothesize that this can be inhibited by including an additional thin interlayer of an

https://doi.org/10.1021/acsnano.2c04786
ACS Nano 2023, 17, 3289–3300

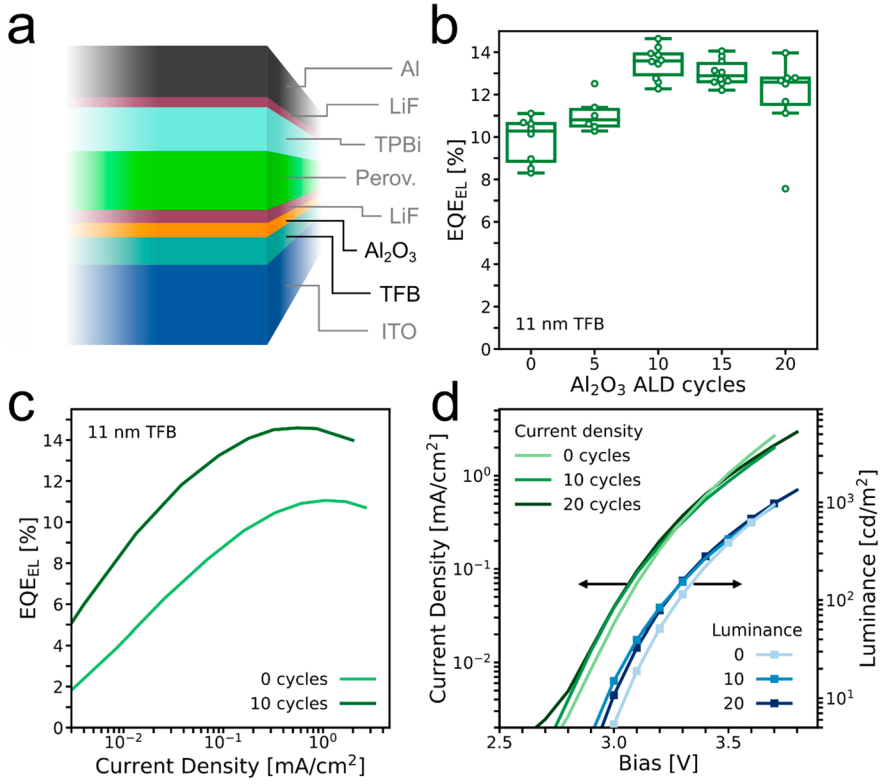

Figure 3. (a) Device schematic of the LEDs with the Al_2O_3 interlayer. (b) EQE_{EL} for each device with varying numbers of ALD cycles. (c) EQE_{EL} as a function of current density for the best-performing device with and without the interlayer from the batch in (b). (d) $J-V-L$ characteristics of the best-performing devices with 0, 10, and 20 cycles from the batch in (b).

electrically insulating material. We proceed to compare with similar electron-only devices where we deposit a thin interlayer of Al_2O_3 via ALD on top of the TFB.

With an ALD-Al_2O_3 layer on top of the TFB in the sandwich between SnO_2 and TPBi (blue boxes in Figure 2e), we see a further reduction in current density across all TFB concentrations. The relative reduction in electron current density due to the Al_2O_3 interlayer is of higher magnitude for the devices with no TFB, where the Al_2O_3 is deposited directly on the SnO_2, and for the thinnest TFB layers.

In the inset in Figure 2e we plot the ratio of the mean of the current densities at 3 V for the Al_2O_3-free and Al_2O_3-processed samples ($\overline{J}_{Free}/\overline{J}_{Al_2O_3}$). Without TFB, the mean current density is 700 times higher without the Al_2O_3 layer than with it. With the thinnest TFB layer, 1.6 nm, the ratio is reduced but remains high at 120. With 3.3 and 11 nm TFB, the Al_2O_3 interlayer reduces the electron current density by factors of 10 and 7, respectively. With a 26 nm TFB layer, the Al_2O_3 layer no longer causes a reduction in current density. In Note 2 in the Supporting Information, we inspect the morphology of the ITO/SnO_2 contact and discuss the relevance of the data from the unipolar, electron-only devices compared to the ITO contact.

Al_2O_3 Interlayer in LEDs. Having seen the reduction in electron leakage current with the ALD-Al_2O_3 interlayer in our unipolar devices, we now incorporate the interlayer into the full LED stack (Figure 3a). First, we make devices with varying numbers of deposition cycles of ALD, where one cycle involves an exposure to TMA and a subsequent exposure to deionized H_2O vapor. We do this on our best-performing structure (11 nm TFB), and a clear increase in the EQE_{EL} with a maximum at 10 deposition cycles is observed (Figure 3b). The average EQE_{EL} rises from 9.8% at 0 cycles to 13.5% at 10 cycles.

The difference in EQE_{EL} between the 0 and 10 ALD cycle samples is significant over the entire current-density range measured (Figure 3c), yet the effect on the $J-V$ curves is small (Figure 3d). This implies that the injected current and series resistance is not strongly influenced by the deposition of the Al_2O_3 interlayer, but the nonradiative current is significantly reduced. See also Note 3 in the Supporting Information.

Using AFM, we also measure the topography of samples of ITO/TFB/Al_2O_3. The effect of the ALD cannot be discerned from the micrographs, where samples with and without the interlayer look similar (Figure S9 in the Supporting Information). We also measure the perovskite layer but do not observe any changes in its morphology that can be attributed to the ALD-Al_2O_3 (Figure S10 in the Supporting Information).

If the ALD-Al_2O_3 layer had formed a dense and continuous layer on top of the TFB, we would expect to see a considerable reduction in current density through the LED, but we do not observe this even at the highest number of cycles tested (Figure 3d). To further our understanding of the impact of this interlayer, we investigated two more configurations, removing the TFB layer and using only ITO/Al_2O_3/LiF as the hole-injection stack (type A) and inserting the Al_2O_3 interlayer under the TFB layer, i.e. depositing the oxide directly on the ITO before spin-coating the polymer ITO/Al_2O_3/TFB/LiF (type B), and compare this with the well-performing ITO/TFB/Al_2O_3/LiF hole-injection stack (type C) with 11 nm TFB and 10 cycles of ALD-Al_2O_3 (Figure 4a,b).

https://doi.org/10.1021/acsnano.2c04786
ACS Nano 2023, 17, 3289−3300

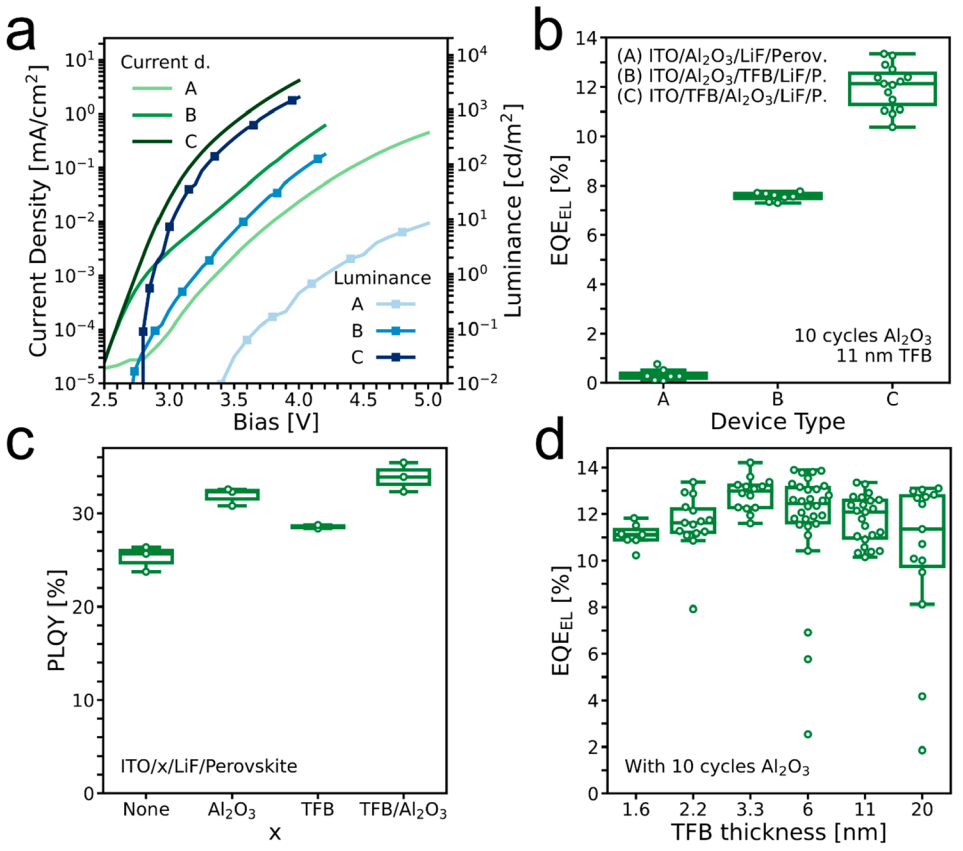

Figure 4. (a) *J*–*V*–*L* characteristics of different configurations of the 10 cycles of Al_2O_3 and 11 nm TFB layers: (i) no TFB HTL, only an Al_2O_3 interlayer; (ii) Al_2O_3 interlayer below the TFB; (iii) Al_2O_3 interlayer on top of the TFB. (b) EQE_{EL} of the same types of devices. (c) PLQY of devices with various layer configurations below the LiF wetting layer. (d) EQE_{EL} as a function of TFB thickness with the Al_2O_3 interlayer in place.

Without the TFB layer (type A), the LEDs have a very high resistance, the current density is reduced by 2 orders of magnitude relative to the control (type C), and the efficiency is below 1%. With the Al_2O_3 directly on the ITO and then TFB above (type B), the current density is increased but is still 1 order of magnitude below that of the control. The luminance of the type B devices is also much higher than that of type A devices but more than 1 order of magnitude lower than the control devices with TFB and then Al_2O_3 (type C). These results suggest that the Al_2O_3 deposition does not form a dense, predominantly continuous, insulating layer when it is applied on top of TFB but does form a more continuous and insulating layer on ITO. Thus, our original configuration still allows efficient hole injection through the TFB to the perovskite emission layer.

We now inspect the effect of 10 cycles of the aluminum oxide interlayer on the PLQY of half-stacks, as shown in Figure 4c, and find an increase of 5% absolute PLQY with the ALD-Al_2O_3 layer processed on top of the 11 nm TFB layer. We also see that the combination of the thin Al_2O_3 and LiF interlayers is able to quite effectively suppress nonradiative recombination at the ITO interface, resulting in high PLQYs.

Now that we have found an effective method to improve our contacts by reducing nonradiative recombination, we try to optimize the LEDs further by varying the TFB layer thickness while keeping the ALD-Al_2O_3 layer constant at 10 cycles. As shown in Figure 4d, the optimum TFB thickness is shifted such that we now find the highest efficiencies in devices prepared with 3.3 nm TFB layers. The champion EQE_{EL} in Figure 4d is 14.2%, but we note that we have reached 15.0% in a 11 nm device with an Al_2O_3 interlayer early in this study (Figure S11 in the Supporting Information) and we therefore expect to be able to obtain even higher efficiencies for this configuration with 3.3 nm TFB and 10 cycles of ALD-Al_2O_3. We note that even the devices with 20 nm TFB show a significant improvement in EQE_{EL} with the Al_2O_3 interlayer (comparing the data presented in Figure 1b and Figure 4d). JVL and $EQE_{EL}(J)$ for the different concentrations with the Al_2O_3 interlayer are given in Figures S12 and S13 in the Supporting Information, respectively. The LED operational stability over time remains largely unchanged by the inclusion of the Al_2O_3 interlayer (Figure S14 in the Supporting Information).

We thus see an improvement in device performance with the Al_2O_3 interlayer across all TFB thicknesses, with a greater change in samples where the TFB coverage is expected to be lower because of the lower thickness. We can attribute this to the difference in growth characteristics of the Al_2O_3 on ITO and on TFB.

In the ALD process of Al_2O_3, the trimethylaluminum precursor reacts with functional groups on the surface to chemisorb on the substrate. In the subsequent steps of the cycle, the gaseous TMA is purged out of the deposition chamber and the second precursor, in this case H_2O, is let into the chamber. The H_2O reacts with the chemisorbed TMA to form a monolayer of aluminum oxide. The nucleation of the Al_2O_3 layer is therefore strongly dependent on the chemistry

https://doi.org/10.1021/acsnano.2c04786
ACS Nano 2023, 17, 3289–3300

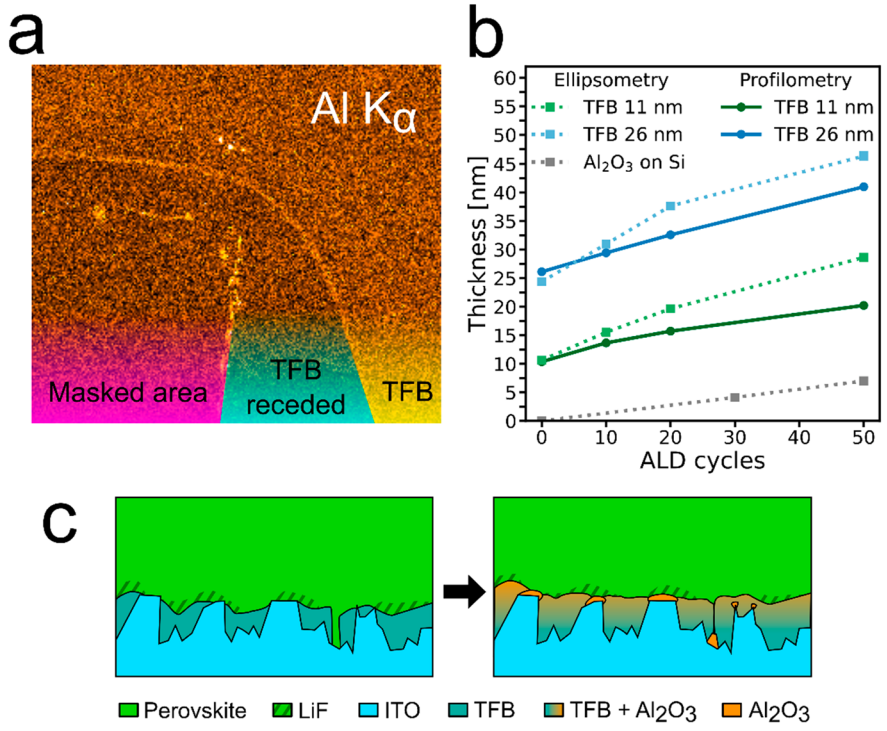

Figure 5. (a) Al Kα counts from EDS mapping over a sample with 11 nm TFB on ITO and then 20 cycles of ALD-Al_2O_3, where a part of the sample was masked by polyimide tape during TFB spin-coating. An increased brightness indicates a higher count intensity. The color coding indicates: (magenta) the area that was masked and is therefore TFB-free, (cyan) an area around the masking tape where the TFB had receded after spin-coating, and (yellow) a TFB-covered area. (b) Thicknesses of TFB-Al_2O_3 samples on Si and Al_2O_3 on Si samples as a function of ALD-Al_2O_3 cycles, where the thicknesses were determined by profilometry (average values) and ellipsometry. (c) Illustration of ALD-Al_2O_3 causing a swelling of the TFB by a,intermixed growth of Al_2O_3, and growth of Al_2O_3 on exposed ITO surfaces. The drawing is not to scale.

between the TMA precursor and the substrate surface. As metal oxides, the surfaces of both ITO and SnO_2 are likely to be terminated by hydroxide groups, which react strongly with TMA. Therefore, a short and effective nucleation phase is expected on these surfaces before the process enters the linear growth phase that is characteristic for Al_2O_3 ALD growth.[43]

On the other hand, many polymers do not possess a high density of functional groups for TMA to bind with and are relatively inert to the ALD nucleation process.[61] Inspecting the molecular structure of TFB (Figure S15 in the Supporting Information), it is clear that there are no −OH, −COOH, or primary amine groups for TMA to react with. TMA, being a strong Lewis acid, could in theory react with the amine group (Lewis base) on the TFB monomer. However, since this is a tertiary amine, it is not expected to be very reactive.

If TMA cannot readily react on the TFB surface, another possibility is for the gaseous TMA molecules to diffuse into micropores within the polymer layer. If, during the following purge, a fraction of the TMA molecules is unable to escape the pores of the TFB, the TMA will then be free to react with H_2O molecules in the next pulse. This would initiate a nucleation and growth of Al_2O_3 particles within the TFB film, effectively resulting in a composite of a TFB matrix infused with Al_2O_3 particles.

To gain an understanding of the growth of the Al_2O_3 interlayer, we performed energy dispersive X-ray spectroscopy (EDS) mapping in SEM on a sample of ITO with 11 nm TFB and 20 cycles of ALD-Al_2O_3, where we masked parts of the substrate with polyimide tape during the TFB spin-coating and then removed the tape to expose this area during ALD. The data are shown in Figure 5a and Figure S16 in the Supporting Information. We see an increased intensity of Al Kα counts in the area with TFB coverage compared to that in areas with just ITO. This implies that there is a larger amount of Al_2O_3 in this area. This suggests we may have some Al_2O_3 growth in the TFB pores.

To further investigate the potential intergrowth of Al_2O_3 within TFB, we deposit TFB and TFB−Al_2O_3 layers on silicon substrates and measure the thickness using both profilometry and ellipsometry (see Figure 5b and Figure S17 in the Supporting Information). We see from Figure S17a,b in the Supporting Information that the thicknesses determined by the two different methods follow each other closely, except at higher ALD cycles the thickness determined by ellipsometry is consistently slightly higher than the average values given by profilometry. Figure S17c in the Supporting Information shows the increase in thickness as a function of ALD cycles relative to the bare TFB (0 cycles). The measured thickness increase exceeds the value expected from linear growth of Al_2O_3 by ALD (1.1 Å per cycle),[43] which would be expected from a continuous film on the TFB surface. In contrast, our deposition of Al_2O_3 directly on a Si substrate with native oxide follows this rate much more closely (Figure S17b,c in the Supporting Information). After 10 cycles, the 11 nm TFB-Al_2O_3 film increases in thickness by 3−5 nm, or 30−50%, relative to the pristine TFB film (Figure S17d in the Supporting Information), much more than the expected 1.1 nm. The layer continues to expand substantially also for 20 and 50 cycles of ALD, and the trend is similar for a thicker pristine TFB film of 26 nm.

https://doi.org/10.1021/acsnano.2c04786
ACS Nano 2023, 17, 3289−3300

From these data, we draw the conclusion that the Al_2O_3 likely grows within pores in the TFB film, resulting in swelling of the TFB layer and the formation of a TFB−Al_2O_3 composite layer. The number of deposition cycles explored in devices in this work (0−20 cycles) is also well within the range considered to be the nucleation phase for growth on many common polymers, before which a conformal linear growth is reached.[39] This could further help explain why there does not seem to be a conformal, insulating blocking layer of Al_2O_3 formed, despite there being a significant volume of Al_2O_3 within the film.

We thus propose that the application of ALD-Al_2O_3 acts by improving the devices in two ways: (1) any uncovered ITO regions on the substrates may be insulated by a more reactive growth in this area, forming a thin but dense and conformal film, and (2) the surface of the TFB is not insulated but the swelling could also act to seal micropores and cause a more continuous surface for subsequent layers in the device fabrication. See the schematic in Figure 5c.

This premise is consistent with the changes we observed for the different LED device configurations. For our "control" devices, incomplete coverage or pinholes in the TFB film lead to nonradiative electron−hole recombination and poor selectivity at the perovskite interface with the ITO (Figure S18a in the Supporting Information). When applying the ALD-Al_2O_3 process, hole conduction through the TFB is sustained, since the Al_2O_3 does not form a dense, continuous layer capping the TFB but rather interpenetrates the polymer. This therefore greatly reduces the electron leakage current, while allowing hole-injection current to flow (Figure S18b,c in the Supporting Information). This confines a higher proportion of the injected electrons to the emitter layer, where they can radiatively recombine with the holes. With the TFB-Al_2O_3 HTL, reduction of the initial TFB thickness, even accounting for swelling post ALD, reduces the hole injection resistance, without the drawback of increased nonradiative recombination from the increasingly large area of exposed ITO surface.

We see an EQE_{EL} increase with 10 cycles of ALD-Al_2O_3 also for the thicker TFB layers (Figure 4d), which is indicative that there could be other positive effects associated with the TFB−Al_2O_3 composite. The composite could have a better energetic alignment compared to that of neat TFB, facilitating improved hole injection into the perovskite layer. Another possibility is that the composite aids in enhancement of the following layer depositions, either the evaporated LiF or the spin-coated perovskite layer. However, our experience with this emission layer indicates that the perovskite crystallization is mostly governed by the 18-crown-6 additive and the presence of the LiF wetting layer.[64] It could also be the case that the reduced HTL thickness has improved the optical outcoupling of the device, though over the layer thickness range (between 3 and 11 nm), which is significantly less than the wavelength of light, we would not expect dramatic changes. A thorough optical model would be needed to confirm this, which is beyond the scope of this work.

This technique, exploiting differences in chemical reactivity of ALD precursors and growth modes between the organic HTL and the underlying TCO to achieve selective insulation of leakage pathways, thus widens the optimization window for device design by expanding the range of viable organic charge transport layer thicknesses that can be used to produce highly efficient devices. In our work, the efficiency gain primarily comes from improved selectivity of the contact. However, in other applications the technique also offers the possibility to optimize the optical outcoupling efficiency through variations of layer thickness without losing carrier selectivity. The combination of an insulator by ALD with an organic charge transport layer may in the future be adapted to other organic charge transport layers, other device architectures, such as n-i-p devices, or other fields such as perovskite photovoltaics. Since ALD systems are common in semiconductor research laboratories, the technique has potential for fast implementation into a large variety of applications. Through commercially available spatial and roll-to-roll ALD systems, the technique should be suitable for scale-up to larger-area LED arrays.[67]

CONCLUSION

The imperfect wetting associated with solution processing can introduce serious spatial inhomogeneities in PeLEDs, presenting a major challenge to scale-up. This challenge is particularly exacerbated by the requirement to have very thin transport layers for the highest efficiencies. Here, we show how ALD can be exploited to improve the quality of the hole-injection layer and contacts, which we rationalize to be due to preferential blocking of regions with pinholes through both swelling of the polymer layer caused by Al_2O_3 growth in the pores of the polymer and preferential Al_2O_3 growth on exposed TCO surfaces, while the polymer surface remains electronically accessible to the perovskite emitter. The improved TFB−Al_2O_3 contact reduces nonradiative recombination sites where there is contact between the degenerately doped ITO and the perovskite emission layer, improving the selectivity of the contact. This allows us to improve the hole injection into the emission layer further by reducing the thickness of the HTL, thus reducing the series resistance for hole injection without introducing additional nonradiative recombination sites. The technique is broadly applicable to a variety of organic transport layers and could expand the optimization window of a variety of devices architectures without a tradeoff in performance due to loss in contact selectivity.

METHODS

Materials. Lead(II) bromide 99.999% (35703, Alfa Aesar), cesium bromide 99.999% (429392, Sigma-Aldrich), 18-crown-6 ≥99.0% (274984, Sigma-Aldrich), TFB (poly(9,9-dioctylfluorene-*alt*-*N*-(4-*sec*-butylphenyl)diphenylamine)), AD259BE, American Dye Source, Inc.), TPBi (2,2′,2″- (1,3,5-benzinetriyl)-tris(1-phenyl-1*H*-benzimadizole, LT-E302, Lumtec Inc.), tin(IV) oxide (44592, Alfa Aesar), LiF (LT-E001, Lumtec Inc.), phenylethylamine (128945, Sigma-Aldrich), ethanol (443611, Sigma-Aldrich), dimethyl sulfoxide (276855, Sigma-Aldrich), chlorobenzene (284513, Sigma-Aldrich), and trimethylaluminum (93−1360, Strem) were all used as purchased without further purification.

PEABr was prepared in-house for a previous project; see Warby et al.[64]

Perovskite Film Fabrication. Perovskite precursor solutions were prepared by weighing out precursor salts in a molar ratio of 5:5:2 of $PbBr_2$:CsBr:PEABr directly into a single vial. DMSO was placed in the vial to a volume corresponding to the $PbBr_2$ salt being at a 0.2 M concentration. The crown ether 18-crown-6 was included in the precursor solution as a structuring agent at a concentration of 4 mg/mL. The solutions were stirred overnight at room temperature and then filtered with a 0.45 μm PTFE membrane filter. Perovskite films were fabricated by spin-coating. The spin-coating program consisted of a first step of 5 s duration at 1000 rpm (1000 rpm/s ramp) followed by a second step of 60 s duration at 3000 rpm (3000 rpm/s ramp). A 100 μL portion of the solution was dispensed onto the spinning substrate 1−2 s into the first step. After the spin-coating

https://doi.org/10.1021/acsnano.2c04786
ACS Nano 2023, 17, 3289−3300

procedure the substrates were immediately moved to a hot plate and annealed for 10 min at 100 °C. All steps took place in a N_2-filled glovebox.

LED Fabrication. Glass substrates with a patterned layer of ITO ($R_s \leq 10\ \Omega$) from Shenzhen Huayu Union technology Co. Ltd. were cleaned by scrubbing with a toothbrush in a solution of deionized (DI) water and Decon 90 detergent. The substrates were then sonicated for a minimum of 3 min per step in the detergent solution, deionized (DI) water, acetone, and isopropanol and then dried using a N_2 gun. Before the deposition of any layers, the cleaned ITO substrates were exposed to a 10 min UV−ozone cleaning process.

TFB solutions were prepared by weighing out TFB powder in a vial and adding chlorobenzene to obtain the desired concentration. The solutions were stirred overnight at 70 °C and then filtered with a 0.22 μm PTFE filter. When testing multiple concentrations, a solution of the highest concentration was made and then diluted into separate vials after filtering to obtain a spectrum of concentrations. TFB layers were spin-coated onto the ITO substrates in ambient air at 4000 rpm for 30 s and then annealed at 120 °C for 10 min.

A homemade ALD system was used to deposit Al_2O_3 at 100 °C. In each cycle, TMA was introduced with a residence time of 5 s before purging for 30 s. DI H_2O vapor was subsequently introduced with a residence time of 5 s and a following purge for 40 s. N_2 was used as both a carrier and purge gas for the process.

LiF was deposited by thermal evaporation in a vacuum chamber positioned in a N_2 glovebox. 2 nm was evaporated for the wetting layer below the perovskite, at a rate of 0.1 Å/s. From this step onward, the samples were kept in an inert atmosphere at all times to prevent reactions with ambient water or oxygen. Perovskite was deposited on LiF-covered substrates by spin-coating as described above.

The samples were again transferred to the thermal evaporator, and a 45 nm layer of TPBi at a rate of 1 Å/s and a 1 nm layer of LiF were evaporated. Then, 80 nm of Al was evaporated at a rate of 1 Å/s using an evaporation mask defining the device layout.

Unipolar Device Fabrication. Unipolar, electron-only devices were fabricated using the same substrates and substrate cleaning procedure as for the LEDs. A 2.67% SnO_2 solution was made by diluting the 15% colloidal dispersion with DI water. The SnO_2 layer was spin-coated onto the ITO substrates using a 30 s spin program at 3000 rpm and dispensing 50 μL of the solution 2 s into the program. The samples were then annealed for 30 min at 150 °C. Before spin-coating TFB on top of the SnO_2, the samples were UV−ozone cleaned for another 10 min to improve wetting. The TFB, Al_2O_3, TPBi, LiF, and Al layers were deposited as described for the LED fabrication.

Sample Fabrication for PLQY. Samples for PLQY measurements were prepared in the same way as for the LEDs for all layers up to the emitter. On the ITO-only sample the perovskite was spun onto the UV−ozone cleaned ITO without a LiF wetting layer. All other layers were deposited as described above. The samples were encapsulated with glass slides bonded on top of the perovskite emitter by use of a Dymax OP-29 UV curing glue, cured for 2 min. The glue was dispensed by a preprogrammed robot, ensuring an optimal dispensing amount and minimal flow into the center of the sample, leaving a large area of pristine perovskite for the PLQY measurements.

Sample Fabrication for Ellipsometry, XRR, and Profilometry. Samples for determination of TFB, TFB-Al_2O_3, and SnO_2 film thicknesses were made on various substrates: ITO, Si, and glass. In each case, the substrate was wet-cleaned as described above for LED fabrication. The substrates were then UV−ozone cleaned (ITO, Si) or plasma cleaned (glass) for 10 min directly prior to spin-coating TFB or SnO_2. TFB or SnO_2 was spun with the same parameters as described for LED fabrication and unipolar device fabrication.

Sample Fabrication for AFM, SEM, and EDS. Samples for AFM and SEM with ITO substrates were prepared following the exact same steps as described for LED devices. Glass substrate samples for AFM were prepared as described above for ellipsometry, XRR, and profilometry. For EDS samples with masking, a polyimide tape was placed across parts of the ITO substrate before TFB spin-coating. A part of the tape was then removed prior to ALD to reveal a TFB-free area. To increase the surface sensitivity and reduce charging of the SEM and EDS samples, a 1 nm layer of Pt or a 5 nm layer of Au was sputtered on top.

EQE_{EL} Measurements. EQE_{EL} measurements were performed using two different setups. The majority of measurements were performed using a calibrated photodiode (Thorlabs FDS 1010) directly above the LED in a N_2 glovebox. This measurement assumed a Lambertian emission profile, the view factor between the photodiode and the LED, and an electroluminescence emission spectrum measured separately using a calibrated grating spectrometer (MayaPro 2000) to calculate the total number of photons emitted. This measurement setup is described in further detail in ref 64.

In addition, some measurements were performed in an integrating sphere with the sample placed in an air-free holder mounted to the side of the sphere. The emission spectrum and intensity were simultaneously measured by an OceanOptics QEPro calibrated grating spectrometer. This setup was used to cross-reference values with the photodiode setup and to measure the spectrum as a function of bias and time.

Both setups measured current density−voltage characteristics using a 2400 series Keithley source-measure unit.

To account for the dynamic nature of PeLED aging, care was taken to measure all samples on comparable time scales since fabrication of the device. Because the PeLEDs age rapidly under bias, each pixel was scanned repeatedly until it had reached its peak efficiency. Only the peak efficiency of each pixel was used to compile the box plots in this publication. This way, differences in efficiency due to difference in aging time could not bias the results.

Unipolar Device Measurements. The unipolar devices were measured with the same setup used for measuring EQE_{EL}. Pixels were scanned from X to $-X$, where X is 3, 5, or 10 V. The first scan on each pixel was used to compile the 3 V snapshot plotted in the paper.

PLQY Measurements. PLQY measurements were carried out in an integrating sphere with encapsulated samples, fabricated as described above, following the procedure of de Mello et al.[68] Lasers with a wavelength of 450 nm were used for excitation; this wavelength was carefully chosen because it is just below the absorption onset of TFB. Two different laser diodes were used: ThorLabs CPS450 and ThorLabs LP1600MM. In each case the intensity on the sample was 47.1 mW/cm^2. The spectrum and intensity of the photoluminescence were measured by an OceanOptics QEPro calibrated grating spectrometer. For each sample, three measurements were taken, each in a different location on the sample. Care was taken each time to ensure the laser spot hit a location within the encapsulated area of the sample. The average PLQYs of the three measurements were then calculated per sample and used as one data point for the analysis and plots in the paper.

Absorbance Measurements. Absorbance of a perovskite film spun directly on a microscope glass slide was measured on a Cary 300 Bio UV−visible spectrometer.

Profilometry Measurements. Profilometry was carried out on a Veeco Dektak 150 profilometer. A razor blade was used to scrape a line in the film, and the profile of the line was measured.

Ellipsometry Measurements. Ellipsometry was carried out on a J.A. Woollam RC2 spectroscopic ellipsometer. Samples were measured at three to five angles between 50 and 75°. In each case, a clean substrate was measured first and used as a foundation for the model of the samples. Fitting was performed in CompleteEASE. The TFB material was fitted by a Cauchy fit in the transparent region, which was then extrapolated into the absorbing region by a B-spline. This gave an excellent fitting result. A Cauchy fit in the transparent region was also used to determine the thickness of SnO_2, again with an excellent fit. For TFB−Al_2O_3 layers, several models were tried, including Cauchy fits in the transparent region, planar bilayers (TFB then Al_2O_3), and Bruggeman effective medium approximations (EMAs) with TFB and Al_2O_3. All methods gave very similar results for the thickness. In the end, a Cauchy fit in the transparent region was used to get the data presented in Figure S17 in the Supporting Information.

https://doi.org/10.1021/acsnano.2c04786
ACS Nano 2023, 17, 3289−3300

XRR Measurements. X-ray reflectivity (XRR) data was acquired with a Rigaku SmartLab diffractometer. This comprised a 1.8 kW (Cu Kα, 1.5406 Å) source with parallel beam optics with a 10 mm length limiting slit and 2.5° Soller slits. The sample were measured from 0 to 4° with a step size of 0.01° in continuous mode. X-ray scattering was collected with a HyPix-3000 2D hybrid pixel-array detector at a sample-to-detector distance of 300 mm. Data was processed using GenX ver. 3.4.11,[69] and the film thickness was fitted as a single-layer polymer layer on the substrate with density and roughness parameters of the substrate and film allowed to float.

SEM and EDS Measurements. Scanning electron microscopy was performed on a FEI Quanta 600 FEG microscope using a secondary electron mode. For top-down measurements, the accelerating voltage was kept as low as possible to reduce penetration depth and enhance surface sensitivity of the low-density polymer surface. EDS was performed in the same SEM, using an x-act detector from Oxford Instruments. EDS was done at 10 keV.

AFM Measurements. Atomic force microscopy measurements were carried out using an Asylum MFP3D microscope in AC (tapping) mode in air. Olympus AC240-TS silicon tips were used for topography measurements.

ASSOCIATED CONTENT

Supporting Information

The Supporting Information is available free of charge at https://pubs.acs.org/doi/10.1021/acsnano.2c04786.

> Emission spectrum of the LEDs, data and procedure for determining the thickness of TFB layers, complementary EQE(J) and J(V) plots for device data presented in the main text, SEM micrographs, device schematics of unipolar devices, morphology considerations of ITO and ITO/SnO_2 contacts, current density statistics of devices with various numbers of ALD cycles, AFM micrographs, layer RMS roughness determined by AFM, EQE(J) plot of the champion device, EQE(time) plot showing stability with and without an Al_2O_3 interlayer, skeletal diagram of the TFB molecular structure, EDS maps of Al_2O_3 on TFB and ITO, and thickness data of TFB-Al_2O_3 mixed layers (PDF)

AUTHOR INFORMATION

Corresponding Author

Henry J. Snaith − *Clarendon Laboratory, Department of Physics, University of Oxford, Oxford OX1 3PU, U.K.;* orcid.org/0000-0001-8511-790X; Email: henry.snaith@physics.ox.ac.uk

Authors

Emil G. Dyrvik − *Clarendon Laboratory, Department of Physics, University of Oxford, Oxford OX1 3PU, U.K.;* orcid.org/0000-0001-7098-615X

Jonathan H. Warby − *Clarendon Laboratory, Department of Physics, University of Oxford, Oxford OX1 3PU, U.K.;* Present Address: Institute of Physics and Astronomy, University of Potsdam, Karl-Liebknecht-Str. 24-25, D-14476 Potsdam-Golm, Germany; orcid.org/0000-0003-3518-173X

Melissa M. McCarthy − *Clarendon Laboratory, Department of Physics, University of Oxford, Oxford OX1 3PU, U.K.;* orcid.org/0000-0003-1512-2046

Alexandra J. Ramadan − *Clarendon Laboratory, Department of Physics, University of Oxford, Oxford OX1 3PU, U.K.;* Present Address: Department of Physics and Astronomy, University of Sheffield, D26, Hicks Building, Hounsfield Road, Sheffield, S3 7RH, U.K.; orcid.org/0000-0003-4572-3459

Karl-Augustin Zaininger − *Clarendon Laboratory, Department of Physics, University of Oxford, Oxford OX1 3PU, U.K.*

Andreas E. Lauritzen − *Clarendon Laboratory, Department of Physics, University of Oxford, Oxford OX1 3PU, U.K.;* orcid.org/0000-0002-1726-7110

Suhas Mahesh − *Clarendon Laboratory, Department of Physics, University of Oxford, Oxford OX1 3PU, U.K.;* Present Address: Edward S. Rogers Sr. Department of Electrical & Computer Engineering, University of Toronto, 10 King's College Rd, Toronto, ON M5S 3G8, Canada.; orcid.org/0000-0002-3897-7963

Robert A. Taylor − *Clarendon Laboratory, Department of Physics, University of Oxford, Oxford OX1 3PU, U.K.;* orcid.org/0000-0003-2578-9645

Complete contact information is available at: https://pubs.acs.org/10.1021/acsnano.2c04786

Notes

The authors declare the following competing financial interest(s): H.J.S. is Co-Founder, Director, and Chief Scientific Officer of Helio Display Materials Ltd.

ACKNOWLEDGMENTS

This work was funded in part by the European Union's Horizon 2020 research and innovation program under grant agreement no. 861985 (PEROCUBE) and ESPRC Prosperity Partnership EP/S004947/1. E.G.D. gratefully acknowledges funding from an Aker Scholarship. S.M. gratefully acknowledges funding from the Rhodes Trust and Schmidt Science Fellows. A.E.L. thanks the EPSRC for funding through the Doctoral Training Partnership EP/N509711/1 as well as the STFC, ISIS Neutron and Muon facility and project 1948713. We also thank Bernard Wenger for helpful advice with the EQE_{EL} measurement setup.

REFERENCES

(1) Lee, M. M.; Teuscher, J.; Miyasaka, T.; Murakami, T. N.; Snaith, H. J. Efficient Hybrid Solar Cells Based on Meso-Superstructured Organometal Halide Perovskites. *Science* **2012**, *338* (6107), 643−647.

(2) Gao, L.; Yan, Q. Recent Advances in Lead Halide Perovskites for Radiation Detectors. *Solar RRL* **2020**, *4* (2), 1900210.

(3) Tan, Z.-K.; Moghaddam, R. S.; Lai, M. L.; Docampo, P.; Higler, R.; Deschler, F.; Price, M.; Sadhanala, A.; Pazos, L. M.; Credgington, D.; Hanusch, F.; Bein, T.; Snaith, H. J.; Friend, R. H. Bright Light-Emitting Diodes Based on Organometal Halide Perovskite. *Nat. Nanotechnol* **2014**, *9* (9), 687−692.

(4) Hu, Z.; Liu, Z.; Zhan, Z.; Shi, T.; Du, J.; Tang, X.; Leng, Y. Advances in Metal Halide Perovskite Lasers: Synthetic Strategies, Morphology Control, and Lasing Emission. *Advanced Photonics* **2021**, *3* (03), 034002.

(5) Yu, X.; Tsao, H. N.; Zhang, Z.; Gao, P. Miscellaneous and Perspicacious: Hybrid Halide Perovskite Materials Based Photodetectors and Sensors. *Adv. Opt Mater.* **2020**, *8* (21), 2001095.

(6) Bowman, A. R.; Anaya, M.; Greenham, N. C.; Stranks, S. D. Quantifying Photon Recycling in Solar Cells and Light-Emitting Diodes: Absorption and Emission Are Always Key. *Phys. Rev. Lett.* **2020**, *125* (6), 67401.

(7) Cho, C.; Zhao, B.; Tainter, G. D.; Lee, J.-Y.; Friend, R. H.; Di, D.; Deschler, F.; Greenham, N. C. The Role of Photon Recycling in Perovskite Light-Emitting Diodes. *Nat. Commun.* **2020**, *11* (1), 611.

(8) Pazos-Outón, L. M.; Szumilo, M.; Lamboll, R.; Richter, J. M.; Crespo-Quesada, M.; Abdi-Jalebi, M.; Beeson, H. J.; Vrućinić, M.;

Alsari, M.; Snaith, H. J.; Ehrler, B.; Friend, R. H.; Deschler, F. Photon Recycling in Lead Iodide Perovskite Solar Cells. *Science (1979)* **2016**, *351* (6280), 1430−1433.
(9) Stranks, S. D.; Hoye, R. L. Z.; Di, D.; Friend, R. H.; Deschler, F. The Physics of Light Emission in Halide Perovskite Devices. *Adv. Mater.* **2019**, *31* (47), 1803336.
(10) Chiba, T.; Hayashi, Y.; Ebe, H.; Hoshi, K.; Sato, J.; Sato, S.; Pu, Y.-J.; Ohisa, S.; Kido, J. Anion-Exchange Red Perovskite Quantum Dots with Ammonium Iodine Salts for Highly Efficient Light-Emitting Devices. *Nat. Photonics* **2018**, *12* (11), 681−687.
(11) Cao, Y.; Wang, N.; Tian, H.; Guo, J.; Wei, Y.; Chen, H.; Miao, Y.; Zou, W.; Pan, K.; He, Y.; Cao, H.; Ke, Y.; Xu, M.; Wang, Y.; Yang, M.; Du, K.; Fu, Z.; Kong, D.; Dai, D.; Jin, Y.; Li, G.; Li, H.; Peng, Q.; Wang, J.; Huang, W. Perovskite Light-Emitting Diodes Based on Spontaneously Formed Submicrometre-Scale Structures. *Nature* **2018**, *562* (7726), 249−253.
(12) Zhao, B.; Bai, S.; Kim, V.; Lamboll, R.; Shivanna, R.; Auras, F.; Richter, J. M.; Yang, L.; Dai, L.; Alsari, M.; She, X.-J.; Liang, L.; Zhang, J.; Lilliu, S.; Gao, P.; Snaith, H. J.; Wang, J.; Greenham, N. C.; Friend, R. H.; Di, D. High-Efficiency Perovskite−Polymer Bulk Heterostructure Light-Emitting Diodes. *Nat. Photonics* **2018**, *12* (12), 783−789.
(13) Hassan, Y.; Park, J. H.; Crawford, M. L.; Sadhanala, A.; Lee, J.; Sadighian, J. C.; Mosconi, E.; Shivanna, R.; Radicchi, E.; Jeong, M.; Yang, C.; Choi, H.; Park, S. H.; Song, M. H.; de Angelis, F.; Wong, C. Y.; Friend, R. H.; Lee, B. R.; Snaith, H. J. Ligand-Engineered Bandgap Stability in Mixed-Halide Perovskite LEDs. *Nature* **2021**, *591* (7848), 72−77.
(14) Soe, C. M. M.; Nagabhushana, G. P.; Shivaramaiah, R.; Tsai, H.; Nie, W.; Blancon, J.-C.; Melkonyan, F.; Cao, D. H.; Traoré, B.; Pedesseau, L.; Kepenekian, M.; Katan, C.; Even, J.; Marks, T. J.; Navrotsky, A.; Mohite, A. D.; Stoumpos, C. C.; Kanatzidis, M. G. Structural and Thermodynamic Limits of Layer Thickness in 2D Halide Perovskites. *Proc. Natl. Acad. Sci. U. S. A.* **2019**, *116* (1), 58−66.
(15) Ban, M.; Zou, Y.; Rivett, J. P. H.; Yang, Y.; Thomas, T. H.; Tan, Y.; Song, T.; Gao, X.; Credgington, D.; Deschler, F.; Sirringhaus, H.; Sun, B. Solution-Processed Perovskite Light Emitting Diodes with Efficiency Exceeding 15% through Additive-Controlled Nanostructure Tailoring. *Nat. Commun.* **2018**, *9* (1), 3892.
(16) Quan, L. N.; Zhao, Y.; García de Arquer, F. P.; Sabatini, R.; Walters, G.; Voznyy, O.; Comin, R.; Li, Y.; Fan, J. Z.; Tan, H.; Pan, J.; Yuan, M.; Bakr, O. M.; Lu, Z.; Kim, D. H.; Sargent, E. H. Tailoring the Energy Landscape in Quasi-2D Halide Perovskites Enables Efficient Green-Light Emission. *Nano Lett.* **2017**, *17* (6), 3701−3709.
(17) deQuilettes, D. W.; Koch, S.; Burke, S.; Paranji, R. K.; Shropshire, A. J.; Ziffer, M. E.; Ginger, D. S. Photoluminescence Lifetimes Exceeding 8 Ms and Quantum Yields Exceeding 30% in Hybrid Perovskite Thin Films by Ligand Passivation. *ACS Energy Lett.* **2016**, *1* (2), 438−444.
(18) Braly, I. L.; deQuilettes, D. W.; Pazos-Outón, L. M.; Burke, S.; Ziffer, M. E.; Ginger, D. S.; Hillhouse, H. W. Hybrid Perovskite Films Approaching the Radiative Limit with over 90% Photoluminescence Quantum Efficiency. *Nat. Photonics* **2018**, *12* (6), 355−361.
(19) Abdi-Jalebi, M.; Andaji-Garmaroudi, Z.; Cacovich, S.; Stavrakas, C.; Philippe, B.; Richter, J. M.; Alsari, M.; Booker, E. P.; Hutter, E. M.; Pearson, A. J.; Lilliu, S.; Savenije, T. J.; Rensmo, H.; Divitini, G.; Ducati, C.; Friend, R. H.; Stranks, S. D. Maximizing and Stabilizing Luminescence from Halide Perovskites with Potassium Passivation. *Nature* **2018**, *555* (7697), 497−501.
(20) Zou, C.; Liu, Y.; Ginger, D. S.; Lin, L. Y. Suppressing Efficiency Roll-Off at High Current Densities for Ultra-Bright Green Perovskite Light-Emitting Diodes. *ACS Nano* **2020**, *14* (5), 6076−6086.
(21) Wang, J.; Wang, N.; Jin, Y.; Si, J.; Tan, Z.-K.; Du, H.; Cheng, L.; Dai, X.; Bai, S.; He, H.; Ye, Z.; Lai, M. L.; Friend, R. H.; Huang, W. Interfacial Control Toward Efficient and Low-Voltage Perovskite Light-Emitting Diodes. *Adv. Mater.* **2015**, *27* (14), 2311−2316.
(22) Shi, Y.; Wu, W.; Dong, H.; Li, G.; Xi, K.; Divitini, G.; Ran, C.; Yuan, F.; Zhang, M.; Jiao, B.; Hou, X.; Wu, Z. A Strategy for Architecture Design of Crystalline Perovskite Light-Emitting Diodes with High Performance. *Adv. Mater.* **2018**, *30* (25), 1800251.
(23) Zhao, L.; Roh, K.; Kacmoli, S.; al Kurdi, K.; Jhulki, S.; Barlow, S.; Marder, S. R.; Gmachl, C.; Rand, B. P. Thermal Management Enables Bright and Stable Perovskite Light-Emitting Diodes. *Adv. Mater.* **2020**, *32* (25), 2000752.
(24) Onno, A.; Chen, C.; Koswatta, P.; Boccard, M.; Holman, Z. C. Passivation, Conductivity, and Selectivity in Solar Cell Contacts: Concepts and Simulations Based on a Unified Partial-Resistances Framework. *J. Appl. Phys.* **2019**, *126* (18), 183103.
(25) Leskelä, M.; Ritala, M. Atomic Layer Deposition Chemistry: Recent Developments and Future Challenges. *Angewandte Chemie - International Edition* **2003**, *42* (45), 5548−5554.
(26) George, S. M. Atomic Layer Deposition: An Overview. *Chem. Rev.* **2010**, *110* (1), 111−131.
(27) Johnson, R. W.; Hultqvist, A.; Bent, S. F. A Brief Review of Atomic Layer Deposition: From Fundamentals to Applications. *Mater. Today* **2014**, *17* (5), 236−246.
(28) Biercuk, M. J.; Monsma, D. J.; Marcus, C. M.; Backer, J. S.; Gordon, R. G. Low-Temperature Atomic-Layer-Deposition Lift-off Method for Microelectronic and Nanoelectronic Applications. *Appl. Phys. Lett.* **2003**, *83* (12), 2405−2407.
(29) Oviroh, P. O.; Akbarzadeh, R.; Pan, D.; Coetzee, R. A. M.; Jen, T. C. New Development of Atomic Layer Deposition: Processes, Methods and Applications. *Sci. Technol. Adv. Mater.* **2019**, *20* (1), 465−496.
(30) Jeong, J.; Laiwalla, F.; Lee, J.; Ritasalo, R.; Pudas, M.; Larson, L.; Leung, V.; Nurmikko, A. Conformal Hermetic Sealing of Wireless Microelectronic Implantable Chiplets by Multilayered Atomic Layer Deposition (ALD). *Adv. Funct Mater.* **2019**, *29* (5), 1806440.
(31) Chang, C. Y.; Lee, K. T.; Huang, W. K.; Siao, H. Y.; Chang, Y. C. High-Performance, Air-Stable, Low-Temperature Processed Semitransparent Perovskite Solar Cells Enabled by Atomic Layer Deposition. *Chem. Mater.* **2015**, *27* (14), 5122−5130.
(32) Yates, H. M.; Afzaal, M.; Walter, A.; Hodgkinson, J. L.; Moon, S. J.; Sacchetto, D.; Bräuninger, M.; Niesen, B.; Nicolay, S.; McCarthy, M.; Pemble, M. E.; Povey, I. M.; Ballif, C. Progression towards High Efficiency Perovskite Solar Cells via Optimisation of the Front Electrode and Blocking Layer. *J. Mater. Chem. C Mater.* **2016**, *4* (47), 11269−11277.
(33) McCarthy, M. M.; Walter, A.; Moon, S.-J.; Noel, N. K.; O'Brien, S.; Pemble, M. E.; Nicolay, S.; Wenger, B.; Snaith, H. J.; Povey, I. M. Atomic Layer Deposited Electron Transport Layers in Efficient Organometallic Halide Perovskite Devices. *MRS Adv.* **2018**, *3* (51), 3075−3084.
(34) Palmstrom, A. F.; Eperon, G. E.; Leijtens, T.; Prasanna, R.; Habisreutinger, S. N.; Nemeth, W.; Gaulding, E. A.; Dunfield, S. P.; Reese, M.; Nanayakkara, S.; Moot, T.; Werner, J.; Liu, J.; To, B.; Christensen, S. T.; McGehee, M. D.; van Hest, M. F. A. M.; Luther, J. M.; Berry, J. J.; Moore, D. T. Enabling Flexible All-Perovskite Tandem Solar Cells. *Joule* **2019**, *3* (9), 2193−2204.
(35) Lin, R.; Xu, J.; Wei, M.; Wang, Y.; Qin, Z.; Liu, Z.; Wu, J.; Xiao, K.; Chen, B.; Park, S. M.; Chen, G.; Atapattu, H. R.; Graham, K. R.; Xu, J.; Zhu, J.; Li, L.; Zhang, C.; Sargent, E. H.; Tan, H. All-Perovskite Tandem Solar Cells with Improved Grain Surface Passivation. *Nature* **2022**, *603* (7899), 73−78.
(36) Kot, M.; Das, C.; Wang, Z.; Henkel, K.; Rouissi, Z.; Wojciechowski, K.; Snaith, H. J.; Schmeisser, D. Room-Temperature Atomic Layer Deposition of Al2O3: Impact on Efficiency, Stability and Surface Properties in Perovskite Solar Cells. *ChemSusChem* **2016**, *9* (24), 3401−3406.
(37) Elam, J. W.; Wilson, C. A.; Schuisky, M.; Sechrist, Z. A.; George, S. M. Improved Nucleation of TiN Atomic Layer Deposition Films on SiLK Low-k Polymer Dielectric Using an Al[Sub 2]O[Sub 3] Atomic Layer Deposition Adhesion Layer. *Journal of Vacuum Science & Technology B: Microelectronics and Nanometer Structures* **2003**, *21* (3), 1099.

https://doi.org/10.1021/acsnano.2c04786
ACS Nano 2023, 17, 3289−3300

(38) Ferguson, J. D.; Weimer, A. W.; George, S. M. Atomic Layer Deposition of Al2O3 Films on Polyethylene Particles. *Chem. Mater.* **2004**, *16* (26), 5602−5609.
(39) Wilson, C. A.; Grubbs, R. K.; George, S. M. Nucleation and Growth during Al2O3 Atomic Layer Deposition on Polymers. *Chem. Mater.* **2005**, *17* (23), 5625−5634.
(40) Groner, M. D.; George, S. M.; McLean, R. S.; Carcia, P. F. Gas Diffusion Barriers on Polymers Using Al 2 O 3 Atomic Layer Deposition. *Appl. Phys. Lett.* **2006**, *88* (5), 051907.
(41) Weber, M.; Julbe, A.; Kim, S. S.; Bechelany, M. Atomic Layer Deposition (ALD) on Inorganic or Polymeric Membranes. *J. Appl. Phys.* **2019**, *126* (4), 041101.
(42) Petit, R. R.; Li, J.; van de Voorde, B.; van Vlierberghe, S.; Smet, P. F.; Detavernier, C. Atomic Layer Deposition on Polymer Thin Films: On the Role of Precursor Infiltration and Reactivity. *ACS Appl. Mater. Interfaces* **2021**, *13* (38), 46151−46163.
(43) Puurunen, R. L. Surface Chemistry of Atomic Layer Deposition: A Case Study for the Trimethylaluminum/Water Process. *J. Appl. Phys.* **2005**, *97* (12), 121301.
(44) Mackus, A. J. M.; Bol, A. A.; Kessels, W. M. M. The Use of Atomic Layer Deposition in Advanced Nanopatterning. *Nanoscale* **2014**, *6* (19), 10941−10960.
(45) Park, K. J.; Doub, J. M.; Gougousi, T.; Parsons, G. N. Microcontact Patterning of Ruthenium Gate Electrodes by Selective Area Atomic Layer Deposition. *Appl. Phys. Lett.* **2005**, *86* (5), 051903.
(46) Chen, R.; Kim, H.; McIntyre, P. C.; Porter, D. W.; Bent, S. F. Achieving Area-Selective Atomic Layer Deposition on Patterned Substrates by Selective Surface Modification. *Appl. Phys. Lett.* **2005**, *86* (19), 191910.
(47) Chen, R.; Bent, S. F. Chemistry for Positive Pattern Transfer Using Area-Selective Atomic Layer Deposition. *Adv. Mater.* **2006**, *18* (8), 1086−1090.
(48) Park, K. S.; Seo, E. K.; Do, Y. R.; Kim, K.; Sung, M. M. Light Stamping Lithography: Microcontact Printing without Inks. *J. Am. Chem. Soc.* **2006**, *128* (3), 858−865.
(49) Suresh, V.; Huang, M. S.; Srinivasan, M. P.; Guan, C.; Fan, H. J.; Krishnamoorthy, S. Robust, High-Density Zinc Oxide Nanoarrays by Nanoimprint Lithography-Assisted Area-Selective Atomic Layer Deposition. *J. Phys. Chem. C* **2012**, *116* (44), 23729−23734.
(50) McDonnell, S.; Longo, R. C.; Seitz, O.; Ballard, J. B.; Mordi, G.; Dick, D.; Owen, J. H. G.; Randall, J. N.; Kim, J.; Chabal, Y. J.; Cho, K.; Wallace, R. M. Controlling the Atomic Layer Deposition of Titanium Dioxide on Silicon: Dependence on Surface Termination. *J. Phys. Chem. C* **2013**, *117* (39), 20250−20259.
(51) Thissen, N. F. W.; Vervuurt, R. H. J.; Mackus, A. J. M.; Mulders, J. J. L.; Weber, J.-W.; Kessels, W. M. M.; Bol, A. A. Graphene Devices with Bottom-up Contacts by Area-Selective Atomic Layer Deposition. *2d Mater.* **2017**, *4* (2), 025046.
(52) Mackus, A. J. M.; Merkx, M. J. M.; Kessels, W. M. M. From the Bottom-Up: Toward Area-Selective Atomic Layer Deposition with High Selectivity. *Chem. Mater.* **2019**, *31* (1), 2−12.
(53) Sinha, A.; Hess, D. W.; Henderson, C. L. Area Selective Atomic Layer Deposition of Titanium Dioxide: Effect of Precursor Chemistry. *Journal of Vacuum Science & Technology B: Microelectronics and Nanometer Structures* **2006**, *24* (6), 2523.
(54) Sinha, A.; Hess, D. W.; Henderson, C. L. Area-Selective ALD of Titanium Dioxide Using Lithographically Defined Poly(Methyl Methacrylate) Films. *J. Electrochem. Soc.* **2006**, *153* (5), G465.
(55) Sinha, A.; Hess, D. W.; Henderson, C. L. A Top Surface Imaging Method Using Area Selective ALD on Chemically Amplified Polymer Photoresist Films. *Electrochem. Solid-State Lett.* **2006**, *9* (11), G330.
(56) Sinha, A.; Hess, D. W.; Henderson, C. L. Transport Behavior of Atomic Layer Deposition Precursors through Polymer Masking Layers: Influence on Area Selective Atomic Layer Deposition. *Journal of Vacuum Science & Technology B: Microelectronics and Nanometer Structures* **2007**, *25* (5), 1721.
(57) Mullings, M. N.; Lee, H.-B.-R.; Marchack, N.; Jiang, X.; Chen, Z.; Gorlin, Y.; Lin, K.-P.; Bent, S. F. Area Selective Atomic Layer Deposition by Microcontact Printing with a Water-Soluble Polymer. *J. Electrochem. Soc.* **2010**, *157* (12), D600.
(58) Park, M. H.; Jang, Y. J.; Sung-Suh, H. M.; Sung, M. M. Selective Atomic Layer Deposition of Titanium Oxide on Patterned Self-Assembled Monolayers Formed by Microcontact Printing. *Langmuir* **2004**, *20* (6), 2257−2260.
(59) Jiang, X.; Bent, S. F. Area-Selective ALD with Soft Lithographic Methods: Using Self-Assembled Monolayers to Direct Film Deposition. *J. Phys. Chem. C* **2009**, *113* (41), 17613−17625.
(60) Huang, J.; Lee, M.; Kim, J. Selective Atomic Layer Deposition with Electron-Beam Patterned Self-Assembled Monolayers. *Journal of Vacuum Science & Technology A: Vacuum, Surfaces, and Films* **2012**, *30* (1), 01A128.
(61) Guo, H. C.; Ye, E.; Li, Z.; Han, M.-Y.; Loh, X. J. Recent Progress of Atomic Layer Deposition on Polymeric Materials. *Materials Science and Engineering: C* **2017**, *70*, 1182−1191.
(62) Yang, X.; Zhang, X.; Deng, J.; Chu, Z.; Jiang, Q.; Meng, J.; Wang, P.; Zhang, L.; Yin, Z.; You, J. Efficient Green Light-Emitting Diodes Based on Quasi-Two-Dimensional Composition and Phase Engineered Perovskite with Surface Passivation. *Nat. Commun.* **2018**, *9* (1), 570.
(63) Futscher, M. H.; Gangishetty, M. K.; Congreve, D. N.; Ehrler, B. Manganese Doping Stabilizes Perovskite Light-Emitting Diodes by Reducing Ion Migration. *ACS Appl. Electron Mater.* **2020**, *2* (6), 1522−1528.
(64) Warby, J. H.; Wenger, B.; Ramadan, A. J.; Oliver, R. D. J.; Sansom, H. C.; Marshall, A. R.; Snaith, H. J. Revealing Factors Influencing the Operational Stability of Perovskite Light-Emitting Diodes. *ACS Nano* **2020**, *14* (7), 8855−8865.
(65) Zhao, B.; Lian, Y.; Cui, L.; Divitini, G.; Kusch, G.; Ruggeri, E.; Auras, F.; Li, W.; Yang, D.; Zhu, B.; Oliver, R. A.; MacManus-Driscoll, J. L.; Stranks, S. D.; Di, D.; Friend, R. H. Efficient Light-Emitting Diodes from Mixed-Dimensional Perovskites on a Fluoride Interface. *Nat. Electron* **2020**, *3* (11), 704−710.
(66) Cho, C.; Greenham, N. C. Computational Study of Dipole Radiation in Re-Absorbing Perovskite Semiconductors for Optoelectronics. *Advanced Science* **2021**, *8* (4), 2003559.
(67) Poodt, P.; Cameron, D. C.; Dickey, E.; George, S. M.; Kuznetsov, V.; Parsons, G. N.; Roozeboom, F.; Sundaram, G.; Vermeer, A. Spatial Atomic Layer Deposition: A Route towards Further Industrialization of Atomic Layer Deposition. *Journal of Vacuum Science & Technology A: Vacuum, Surfaces, and Films* **2012**, *30* (1), 010802.
(68) de Mello, J. C.; Wittmann, H. F.; Friend, R. H. An Improved Experimental Determination of External Photoluminescence Quantum Efficiency. *Adv. Mater.* **1997**, *9* (3), 230−232.
(69) Björck, M.; Andersson, G. GenX: An Extensible X-Ray Reflectivity Refinement Program Utilizing Differential Evolution. *J. Appl. Crystallogr.* **2007**, *40* (6), 1174−1178.

https://doi.org/10.1021/acsnano.2c04786
ACS Nano 2023, 17, 3289−3300